Key Points:
- Sentinel-1A InSAR and GPS results reveal rainfall-triggered landslide-body surface subsidence prior to downslope sliding
- 3D deformation measurements provide insights on the temporal and spatial complexity of landslide dynamics
- Spaceborne InSAR-derived displacement fields can be used to invert for active landslide thickness variation based on mass conservation

Combining InSAR and GPS to Determine Transient Movement and Thickness of a Seasonally Active Low-Gradient Translational Landslide

Xie Hu[1] (ID), Zhong Lu[1] (ID), Thomas C. Pierson[2] (ID), Rebecca Kramer[2] (ID), and David L. George[2] (ID)

[1]Huffington Department of Earth Sciences, Southern Methodist University, Dallas, TX, USA, [2]U.S. Geological Survey, Vancouver, WA, USA

Abstract The combined application of continuous Global Positioning System data (high temporal resolution) with spaceborne interferometric synthetic aperture radar data (high spatial resolution) can reveal much more about the complexity of large landslide movement than is possible with geodetic measurements tied to only a few specific measurement sites. This approach is applied to an ~4 km^2 reactivated translational landslide in the Columbia River Gorge (Washington State), which moves mainly during the winter rainy season. Results reveal the complex three-dimensional shape of the landslide mass, how onset of sliding relates to cumulative rainfall, how surface velocity during sliding varies with location on the topographically complex landslide surface, and how the ground surface subsides slightly in weeks prior to downslope sliding.

1. Introduction

The three-dimensional (3D) geometry and movement of landslides, particularly large landslides, can be complex and difficult to characterize. Conventional stability analyses (e.g., Rogers & Chung, 2016) require estimates of depth to the basal slip surface and material properties, which are usually obtained from field investigations at a few specific locations. Acquisition of such data typically involves expensive drilling or excavation at a limited number of locations, and properties between holes can only be interpolated. Furthermore, some landslide sites may be hazardous to work on and/or inaccessible.

Existing noncontact methods for determining failure surface geometry and landslide volume, such as the balanced cross-section method (e.g., Aryal et al., 2015; Bishop, 1999), the dislocation model (e.g., Aryal et al., 2015; Nikolaeva et al., 2014), and the mass conservation approach (Booth et al., 2013; Delbridge et al., 2016; Huang et al., 2017), require only an analysis of 3D displacement maps. However, these methods vary in their accuracy based on the underlying model assumptions: the balanced cross-section method considers multiple cross sections independently without taking adjacent bodies into account, and the dislocation model largely simplifies the landslide geometrically and physically, employing a linear elastic model and a single rectangle planar basal surface (Nikolaeva et al., 2014). Alternatively, the mass conservation approach used to map glacier ice thickness (Farinotti et al., 2009; Morlighem et al., 2011) has been extended to landslide thickness inversions (Booth et al., 2013; Delbridge et al., 2016; Huang et al., 2017). The accuracy of these noncontact methods is limited to the accuracy of the utilized 3D displacement fields.

Spatially continuous 3D displacement fields can be constructed by geodetic methods such as differential digital elevation models (DEMs), pixel offset tracking using optical or synthetic aperture radar (SAR) images, and interferometric SAR (InSAR) when three or more measurements of independent imaging geometries are available. Application of these methods still presents challenges.

The differential DEM method requires repeat high-resolution DEMs, such as bare-earth light detection and ranging DEMs, which are not commonly available for landslide areas. The pixel offset tracking methods estimate deformation using pixel shifts, detected by searching for the cross-correlation peak between the matching patches of two images (e.g., Michel et al., 1999; Scambos et al., 1992). Optical images can be used for pixel offset tracking, but landslides are generally located in vegetated hilly terrain, so that ground features are difficult to distinguish with optical data. SAR electromagnetic waves can penetrate vegetation to a certain degree (depending on the wavelength and characteristics of canopies such as thickness and moisture), making SAR data better for pixel tracking than optical data. However, spaceborne SAR data have large pixel

spacings (several to dozens of meters). Pixel offset tracking is only applicable when the displacement exceeds ~1/10 of the pixel spacing between two temporal acquisitions (Hu et al., 2014; Wang & Jónsson, 2015), such as for the Slumgullion landslide, Colorado, where movement is as high as ~2 cm/day (Delbridge et al., 2016). Thus, the deformation magnitude of slow-moving landslides, mostly less than tens of centimeters per year (e.g., Mackey & Roering, 2011), is generally too small for detection by pixel tracking and not appropriate for this study.

InSAR methods determine deformation from the differential phase shift of reflected radar waves returning to the sensor in temporally spaced data acquisitions. But general limitations of the methods include the geometric distortion due to topographic relief and poor coherence due to vegetation (e.g., Hu et al., 2016). Spaceborne InSAR is additionally limited by significant insensitivity to north-south motion due to line-of-sight (LOS) slant-looking geometries of near-polar-orbiting SAR satellites. Airborne InSAR methods (such as radar sensors mounted in unmanned aerial vehicles—UAVSAR systems) have the advantages of high-resolution detection (submeter to meter level), and they are not restricted to the fixed-looking geometries (allowing the detection of north-south motion) (Delbridge et al., 2016). However, airborne SAR data seldom cover large areas, and data availability is generally restricted due to agreements between service providers and clients.

Decrease in effective shear strength along basal shear surfaces due to increased pore pressure from infiltrated rainwater (or snowmelt) is a major trigger of landsliding (Iverson et al., 2000; Iverson et al., 1997). The correlation of landslide movement with seasonal rainfall in the study area of the Crescent Lake landslide (Hu et al., 2016; Tong & Schmidt, 2016) indicates that it is the operative trigger mechanism. But rainfall-triggered landslide movement, particularly the time of failure and extent of displacement and runout, is typically difficult to predict, because (a) the fluid pressure evolution is complex, owing to the combined effect of groundwater inflow and infiltration and to variations in subsurface flow paths due to the heterogeneous soil matrix at and above the basal slip surface (Iverson, 2000; Iverson et al., 1997); (b) landslide movement is highly sensitive to the initial soil porosity and can result in contrasting dynamics upon shearing (Iverson et al., 1997; Iverson et al., 2000); and (c) the time required for infiltration and pressure transmission to elevate the pressure head at the basal shear zone is uncertain (Iverson, 2000; Priest et al., 2011).

In this study, we apply a method using ascending- and descending-track InSAR measurements, constrained by the topographic slope, to first derive the long-term quasi-3D displacement fields for a large seasonally slow-moving landslide, and then to invert for active landslide thickness (Booth et al., 2013). Our analysis reveals a basal slip surface that is more irregular than might be expected for a translational landslide thought to be sliding on bedding-parallel surfaces within a sedimentary deposit. Together with the on-slide continuous Global Positioning System (GPS) measurements, geodetic InSAR observations reveal an unexpected precursory subsidence of the landslide surface before downslope sliding begins.

2. Study Area and Data

The Washington side of the Columbia River Gorge is especially prone to landslides due to weak underlying volcaniclastic sedimentary units that dip toward the river at 2°–10°, a wet winter climate, and steep unbuttressed slopes. Approximately two thirds of this terrain in the western Columbia Gorge comprises old or currently active, mostly translational landslides (Pierson et al., 2016). The infiltration of winter rainfall and snowmelt elevates pore-water pressure and reduces frictional strength at a number of potential failure surfaces at different levels within the volcaniclastic units, resulting in landside reactivation (Handwerger et al., 2015; Mackey & Roering, 2011). The focus of this study is the ~4 km^2 Crescent Lake landslide (Figure 1), a translational landslide in Skamania County just west of Stevenson, Washington (Pierson et al., 2016). The landslide moves mainly during the winter, much of it at an average rate of 15–20 cm/year (Hu et al., 2016; Tong & Schmidt, 2016), and it has been active for at least several decades (Braun et al., 1998).

The Crescent Lake landslide, with an average surface slope of 10–11% (6°) facing southeast, is a reactivated portion of the less than 600 years old Red Bluffs landslide within the ~36 km^2 Cascade landslide complex. All of the Cascade complex slides are composed of poorly sorted coarse landslide debris (blocks up to at least many tens of meters in diameter), derived from Quaternary lavas of andesite and basaltic andesite composition, thick lavas of the middle Miocene Columbia River Basalt group, and lahar and coarse fluvial deposits (andesite and dacite particles) of the lower Miocene Eagle Creek Formation and the upper Oligocene Weigle Formation (informal name) (Palmer, 1977; Pierson et al., 2016; Randall, 2012; Wise, 1961). Clay-rich
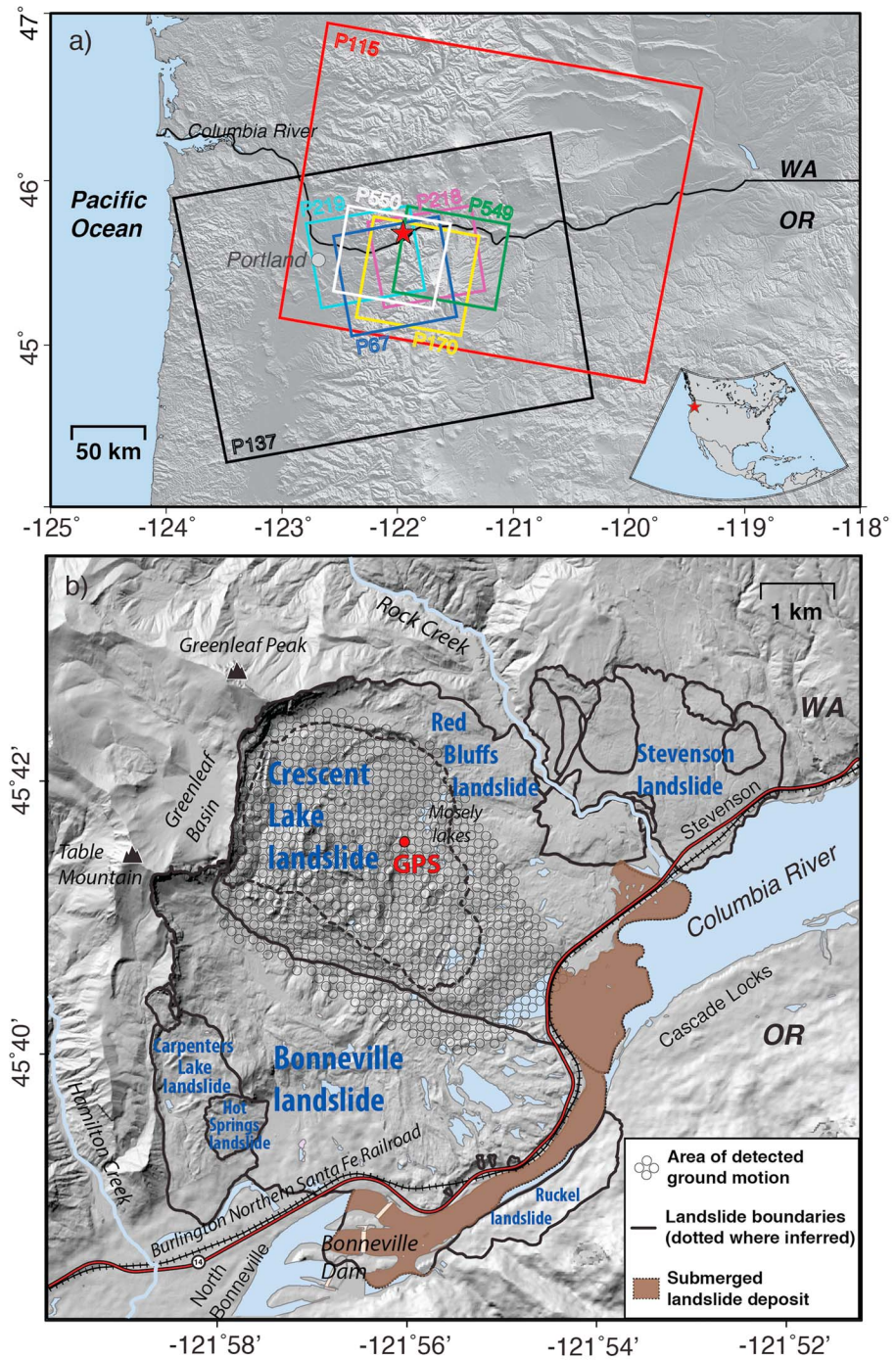
Figure 1. Location maps of study area: (a) synthetic aperture radar data coverage and (b) shaded relief map of the Cascade landslide complex (Pierson et al., 2016), with dashed outline of Crescent Lake landslide determined by geomorphic evidence and early interferometric synthetic aperture radar interferograms. The solid black lines show other landslides within the complex. The shaded area (covered by the array of circles) encompasses the area of detected movements (Hu et al., 2016), downsampled to 100 m by 100 m grids for smoothness preservation; it is the area used for thickness inversion. The red dot marks the location of the continuous Global Positioning System station that provided the data for this study.

weathering horizons developed throughout the lower parts of Eagle Creek Formation and the upper parts of Weigle Formation are believed to be the failure surfaces for most landslides in this area (Palmer, 1977; Pierson et al., 2016; Randall, 2012; Waters, 1973), including the Crescent Lake landslide. The Crescent Lake landslide has not been drilled to determine thickness, but the adjacent Bonneville landslide (Figure 1) has a maximum

thickness of about 150 m and an average thickness of about 76 m (Pierson et al., 2016), based on a cross section determined by drilling (Palmer, 1977).

The Crescent Lake landslide is covered with forest vegetation that is moderate to sparse in coverage density. This makes it compatible with SAR analysis, which can readily reveal creeping landslide motion in areas larger than 0.2 km^2 with limited vegetation cover (Zhao et al., 2012). Previous InSAR results of ALOS-1 Phased Array type L-band Synthetic Aperture Radar 1 (PALSAR-1) data suggested a cumulative ~0.7 m slope-parallel displacement of the Crescent Lake landslide during 2007–2011 (Hu et al., 2016). However, the basal geometry at depth and its movement timing had not been investigated in the prior study. To reveal details of ground deformation and to invert for landslide body thickness, we collected multiple spaceborne SAR data, including two ascending tracks (P218 and P219 data) and two descending tracks (P549 and P550 data) acquired by ALOS-1 PALSAR-1 from 2007 to 2011, one ascending track (P67 data) and one descending track (P170 data) acquired by ALOS-2 PALSAR-2, and one ascending track (P137 data) and one descending track (P115 data) acquired by Sentinel-1A from the end of 2014 to 2016 (Figures 1a and S1).

3. Methods

3.1. Mapping a Quasi-3D Creeping Landslide Using Spaceborne InSAR Observations

The Crescent Lake landslide primarily moves to the southeast horizontally. However, spaceborne InSAR observations are largely insensitive to north-south motion, regardless of the orbit direction (ascending or descending). For InSAR available at Crescent Lake landslide, the radar heading angle is ~ −10° and the looking direction is ~80° for ascending data, which is nearly orthogonal to the slope aspect (~170°) at the lower southeast section of the landslide (Figure S2). Therefore, the motion in this part of the landslide is nearly undetectable. Four ascending/descending tracks of SAR data sets were used for each observation time period. The InSAR time-series processing method detailed in Hu et al. (2016) was used to process ALOS-1 and Sentinel-1A data sets. For the other data sets with limited number of images, we used averaging/stacking to obtain their LOS velocity. Data from ascending tracks share one radar-imaging geometry, and data from the descending tracks share another. Therefore, there are essentially two independent measurements for each time period, making it difficult to constrain the complete 3D displacement fields. We therefore assume that the long-term surface movement is exclusively downslope in the direction of slope aspect on the slope-parallel basal surface under the force of gravity; that is, motion in the cross-slope direction (*v*) is negligible (Figure S3). This assumption is supported by the observed GPS data, which indicate that *v* is much smaller than *u* (Figure 2). Given this constraint, we can obtain the quasi-3D displacement fields (see the supporting information).

3.2. Landslide Thickness Inversion

Landslide thickness can be determined from the governing equation for mass conservation, given the assumption of incompressibility, which requires the 3D velocity field to be divergence-free ($\nabla \cdot \mathbf{V} = 0$). By vertically integrating this equation between the basal slip surface and upper surface, and applying kinematic boundary conditions, a two-dimensional governing equation is derived,

$$\frac{\partial h}{\partial t} + \nabla \cdot (h\overline{\mathbf{v}}) = 0 \tag{1}$$

where *h* is the landslide thickness, *t* is time, and $\overline{\mathbf{v}} = (v_x, v_y)$ is the depth-averaged horizontal velocity, which can be related to the surface horizontal velocity $\mathbf{v_{surf}}$ by $\overline{\mathbf{v}} = f \cdot \mathbf{v_{surf}}$, where *f* depends on rheological assumptions and ranges from 0 to 1. We further assume that the rheology of the landslide body is spatially uniform, yielding a constant *f* that can be expressed as $f = 1 - \frac{Y}{3(Y+P)}$, where *Y* and *P* are the thickness of the lower yield zone and overlying plug region, respectively (Figure S3) (Delbridge et al., 2016). For the case of a power law rheology, *f* = 1/2 corresponds to a linear vertical velocity profile; *f* = 2/3 corresponds to Newtonian viscous flow, such that the entire depth has yielded and the plug region vanishes; 2/3 < *f* < 1 indicates plug flow (with a thin yield zone); and *f* = 1 implies a rigid sliding block with no yield zone (Booth et al., 2013). While the inverted thickness is affected by the rheological parameter, the spatial pattern of thickness is unaffected by the uniform value of the parameter *f* (Delbridge et al., 2016).

Assuming that the landslide basal surface does not change over the observation period, the rate of thickness change is equivalent to the vertical surface velocity, v_z. Equation (1) can then be written as
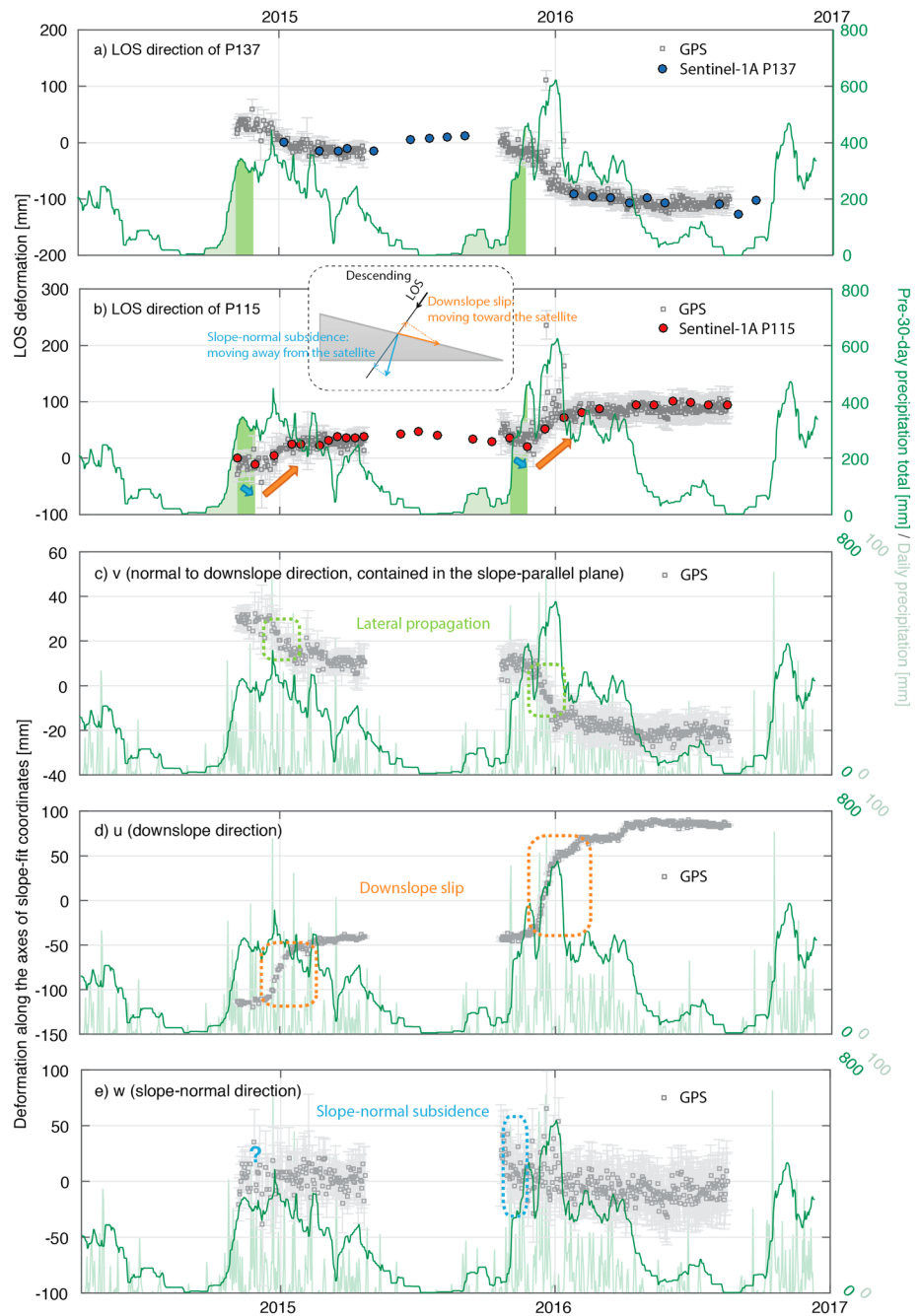
Figure 2. Global Positioning System (GPS) displacements at the semipermanent GPS station (red dot in Figure 1) projected onto the LOS direction in comparison with the Sentinel-1A measurements of (a) ascending track P137 and (b) descending track P115, along with pre-30 day precipitation total (30 day cumulative precipitation before the assigned date) from a nearby weather station (Cascade Locks, Oregon). The light green shading under the pre-30 day precipitation curves shows the antecedent rainfall period, and the dark green shading corresponds to the period of slope-normal subsidence when the precipitation is more intense. The inset diagram shows how ground displacement is sensed by a right-looking satellite on a descending track. (c–e) GPS measurements with the corresponding components on u, v, and w directions based on the slope-fit coordinate system, along with pre-30 day and daily precipitation records.

$$v_z = -f\nabla \cdot (h\mathbf{v}_{surf})$$

(2)

We invert for h by using the nonnegative least squares method (Booth et al., 2013; CVX Research, Inc., 2013). We set the upper threshold as 150 m at this site based on the thickness of an adjacent landslide (Pierson et al.,

2016). The boundary condition is that the landslide thickness vanishes at its lateral boundaries (see the supporting material for details of the solution procedure).

4. Results

4.1. Validation of InSAR Results Using GPS Data

We have acquired partially continuous GPS data from a station located in the central part of the Crescent Lake landslide (red dot in Figure 1b) for two periods between late 2014 to mid-2016; data were missing during the summer months of 2015 (Figure S4). The semipermanent GPS station (Dzurisin et al., 2017) is mounted in ~5 m block of rock "floating" in landslide debris and sits at an elevation of 260 m, where the landslide has a local average slope angle of 9° and a slope aspect of 100° (measured clockwise from 0° at the north; Figure S2). Comparing the LOS displacements of Sentinel-1A data to that derived by GPS (Figure 2) suggests a good agreement with an average root-mean-square deviation of 5.68 and 10.11 mm for P137 and P115, respectively. The orbit of P115 is descending, and the active lobe moves toward the satellite along the slant range, in contrast to the results of ascending orbit of P137.

The high temporal resolution of Sentinel-1A data reveals a peculiar signal in the early part of the wet season (primarily November): apparent upslope or slope-normal downward motion, which is also seen in the GPS data, particularly in late 2015. To further investigate this anomalous movement, we transform the GPS measurements to the slope-fit coordinates (see Figure S3 for the coordinate systems and Figures 3c–3e for GPS results). Generally, v (normal to slope aspect and contained in the slope-parallel plane) is approximately northward, u (slope aspect of the largest topographic gradient) is approximately eastward, and w (normal to slope plane) is approximately upward. The precursory motion does not show in the u component, indicating that there is no actual upslope motion; the phase change is detectable only in v component. However, the magnitude is only around 10 mm, much less than what is expressed in LOS by nearly 50 mm. These results suggest that the early wet season signal must be the result of subsidence.

The precursory slope-normal subsidence and the subsequent downslope movement of the landslide mass have been clearly captured by the descending Sentinel-1A satellite. This is because slope-normal subsidence corresponds to slant range increase (movement away from the satellite), and the downslope motion corresponds to slant range decrease (movement toward the satellite). The descending LOS measurements pick up the motions well, because the satellite LOS is looking nearly straight at the direction of oncoming landslide motion.

4.2. Quasi-3D Displacement Maps

We use the estimated LOS velocity of each data set (Figure S5) to define the quasi-3D displacement field (horizontal and vertical movements) for the Crescent Lake landslide (Figures 3a–3c). Horizontal motion over much of the landslide, shown by velocity vectors, is divergent away from the approximate center line of the landslide. Along the southwest margin of the slide, motion is primarily to the south and deviates nearly 45° from the average direction of movement. Along this margin the Crescent Lake landslide appears to be overlapping onto the older Bonneville landslide deposit, based on the morphologic appearance of this lateral margin (Pierson et al., 2016) and on an abrupt change in landslide thickness along a lineament, where velocity changes direction and magnitude (Figure 3). Vertically, localized subsidence is clearly evident across the entire upper part of the landslide (particularly in 2007–2011), and along much of the southwest margin. Additionally, several localized zones near the mapped toe of the landslide exhibit some localized uplift. Uplift along the northeast margin during 2007–2011 (but with different vertical motion in 2014–2016) might reflect tilting of one or more large slide blocks.

4.3. Active Landslide Thickness

The inversion results indicate that Crescent Lake landslide is thickest (assumed up to 150 m) in a wide band across the middle of the landslide that strikes across the topographic surface slope (Figure 3). The area outside of the active slide on the southwest margin has been masked out (cross-hatched zone in Figures 3d–3f). Within the boundaries of the mapped landslide (solid line in Figures 3d–3f), the thick zone terminates abruptly against a southeasterly trending subsurface escarpment (immediately left of the dashed line). Longitudinally, the landslide thins toward its head and its toe areas.
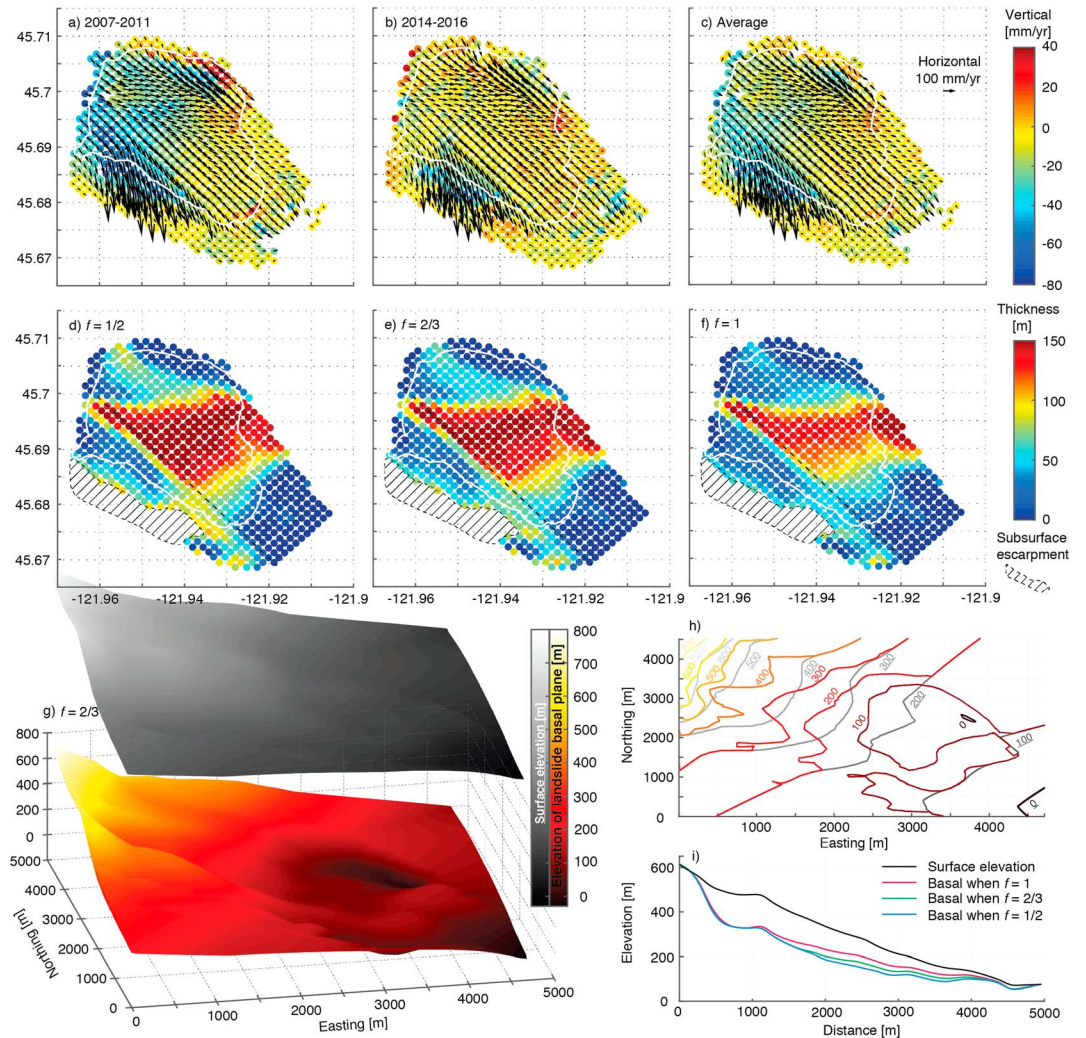
Figure 3. Thickness variation of the Crescent Lake landslide, obtained by inversion of the quasi-3D displacement field. Quasi-3D displacement velocity maps in unit of mm/year during (a) 2007–2011, (b) 2014–2016, and (c) the average of 2007–2011 and 2014–2016 of the shaded zone shown in Figure 1. The horizontal velocity vectors indicate direction (effectively imposed by topographic slope) and magnitude of horizontal displacements, and the color shows magnitude of vertical displacements. Thickness is shown in meters when (d) $f = 1/2$, (e) $f = 2/3$, and (f) $f = 1$, respectively. The solid line shows the mapped boundary of the Crescent Lake landslide (Pierson et al., 2016), and the cross-hatched zone marks the area outside of the southwest margin of the landslide. (g) Geometry of the smoothed landslide top surface and basal surface when $f = 2/3$. Note that the boundaries of the topographic ground surface and the basal surface are superimposed, but the topographic ground surface is raised to better reveal the basal surface variations. (h) Elevation contours of the smoothed slope surface (gray lines and underlined digits) and the basal surface (colored lines and digits). (i) Profiles of surface elevation and landslide basal surface elevations along the dashed line transect.

Use of a larger f value (more plug region and less yield zone) yields smaller thicknesses for the same displacement fields. Our results render landslide volume estimates of 6.6×10^8, 7.8×10^8, and 8.2×10^8 m^3 for f value equals to 1, 1/2, and 2/3, respectively, and assuming a maximum thickness of 150 m and unbiased slope and aspect angles (Table S1). Our results are on the same order as the estimated volume (6.5×10^8 m^3) of the active part of the Red Bluff landslide (i.e., the Crescent Lake landslide) by Randall (2012). The inversion-derived basal surface is hummocky (Figures 3g and 3h). This is realistic because most of the landslides in this area have slid onto hummocky deposits of older landslides (Pierson et al., 2016). We obtain a longitudinal thickness profile of the landslide (transect at dashed line) by determining the elevation of the basal surface as the smoothed surface elevation minus the derived thickness (Figure 3i). Surface slope aspect along this transect is fairly uniform. The dependence of basal surface depth on f is more pronounced in the downslope part of the profile.

5. Discussion and Conclusions

The Crescent Lake landslide is a moderately large (~4 km^2), seasonally active, translational landslide in forested terrain, the motion of which would be difficult to characterize using standard geophysical methods. We have used spaceborne InSAR analysis to augment data from a semipermanent GPS station to track motion of the landslide over two wet seasons. InSAR analysis offers major advantages in characterizing kinematics of a complex landslide: (a) motion of the whole landslide can be evaluated, not just motion at a few points; (b) temporal and spatial resolution of variations in motion can be determined at a weekly or biweekly scale that allows the transient movements to be captured; and (c) variations in landslide thickness can be determined by ground displacement measurements at a scale that allows the complexity of the landslide basal surface to be characterized.

We propose a method to derive quasi-3D displacement fields using two independent spaceborne InSAR measurements (ascending and descending) that could have applications for studying other deforming bodies (glaciers, volcanic cones, natural dams, etc.). Determination of displacement fields also allows variations in active landslide thickness to be approximated, based on mass conservation and assuming a homogeneous deforming mass. Depth-averaged horizontal velocities are approximated from surface velocities using the rheological parameter f. The assumption of downslope motion, taking as the reference for the derivation of quasi-3D displacements, is in essence based on the topography, or more specifically, the angles of slope and aspect at each target. Assuming that the uncertainty of slope and aspect is in ±3°, the consequent landslide average thickness and volume (e.g., $f = 2/3$) can vary by about 8% (Table S1), yet the spatial patterns of landslide thickness are not changed much (Figure S6). In addition to the input displacement maps, the thickness approximations depend on (a) choice of the rheological parameter f, which is essentially a scaling factor; (b) assigned landslide areas and boundary conditions, which assert that the landslide thickness and motion vanish at the lateral margins; and (c) a priori knowledge or estimation of maximum landslide thickness. Our results show that the thickest part of Crescent Lake landslide is approximately in the middle and that there are abrupt changes in thickness, likely reflecting underlying topography.

Spatial variations in surface movement of the landslide are complex. The field of InSAR-derived ground-surface movement is larger than the previously mapped area of the landslide, which was defined on the basis of geomorphic features visible in light detection and ranging imagery (Pierson et al., 2016). Variable amounts of subsidence during sliding occur primarily in the upper half of the landslide body, which correlates strongly with zones of accelerated horizontal movement. Accelerated sliding is also evident along the southwest lateral margin, where the landslide laps onto the older Bonneville landslide deposit and thins substantially. Horizontal surface motion vectors vary in magnitude from nearly zero to about 350 mm/year and vary in direction by nearly 90°.

Temporal variations in slide movement are also complex at the GPS station location in the middle of the landslide body. Under proper configuration between radar looking geometry and slope geometry, InSAR LOS observations may provide a unique perspective to better differentiate motions at different directions. Not only is the onset of seasonal downslope sliding detected using Sentinel-1A data but a multi week period of ground subsidence prior to the onset of sliding is also detected. Pronounced subsidence began early in the rainy season after ~140 mm of antecedent rainfall accumulated. Once a total of ~270 mm of rain had accumulated, major downslope sliding began (Figure 2 and Table S2).

The reason for the apparent presliding surface subsidence is uncertain. It could be due to elastic ground loading deformation in response to the accumulating mass of infiltrated rainfall (Fu et al., 2015; Hu et al., 2016), which from the InSAR data arguably could have started at the beginning of the fall rain in 2016. In loose soils subjected to shear stress, contractive soil behavior can occur during wetting or incipient motion (Iverson et al., 2000), and this can cause subsidence. Such contraction of saturated granular soil causes pore pressure at the failure surface to be rapidly elevated, and this, in turn, leads to abrupt decreases in shear strength that can trigger runaway acceleration (Iverson, 2005; Iverson et al., 2015). But contractive soil behavior is unlikely in this case, because where subsidence was detected, the slip surface is deep (~100 m) and subject to high normal stress, the soil material is chemically altered and clay-rich, and slip has been occurring intermittently for decades. Given these constraints, shear has almost certainly reduced porosity and strength at the slip surface to a residual state in which further contraction is highly unlikely.

The observed seasonal creep of this landslide argues for the opposite of contractive behavior—dilatant soil behavior. Dilatant strengthening during shear in already compact granular material leads to slow, limited shear in landslides (Iverson, 2005; Moore & Iverson, 2002). If critical-state porosity is never reached during shear and if recompaction occurs during periods of no shear, episodes of slow shear can regularly recur, as we observe at the Crescent Lake landslide. The observation that slip in this landslide occurs at its fastest rate initially, followed by a long period of deceleration (Figure 2), suggests that shear strength gradually increases during shear after the initial release. This mechanism would theoretically cause the ground surface to rise, not subside, so further investigation is needed to explain the direction and magnitude of observed ground-surface movement prior to the onset of downslope sliding.

This study has shown that the combined application of continuous GPS data having high temporal resolution with spaceborne InSAR data having high spatial resolution can reveal much more about the complexities of large landslide 3D shape and movement than is possible with geodetic measurements tied to only a few specific measurement sites. It shows the variations in landslide thickness and the configuration of the basal slip surface. It allows timing of the onset of sliding and the rate of sliding to be linked with threshold intensities and durations of rainfall. It allows spatial variations in sliding direction and rate to be assessed. And it also allows interannual differences in landslide behavior to be assessed in light of year-to-year variations in rainfall and other climatic factors.

References

Aryal, A., Brooks, B. A., & Reid, M. E. (2015). Landslide subsurface slip geometry inferred from 3-D surface displacement fields. *Geophysical Research Letters*, *42*, 1411–1417. https://doi.org/10.1002/2014GL062688

Bishop, K. M. (1999). Determination of translational landslide slip surface depth using balanced cross sections. *Environmental and Engineering Geoscience*, *5*(2), 147–156.

Booth, A. M., Lamb, M. P., Avouac, J.-P., & Delacourt, C. (2013). Landslide velocity, thickness, and rheology from remote sensing: La Clapière landslide, France. *Geophysical Research Letters*, *40*(16), 4299–4304. https://doi.org/10.1002/grl.50828

Braun, J., Major, G., West, D. O., & Bukovansky, M. (1998). Geologic hazards evaluation boosts risk-management program for Western U.S. pipeline. *Oil & Gas Journal*, *96*(45), 13.

CVX Research, Inc. (2013). CVX: Matlab software for disciplined convex programming, version 2.0 beta.

Delbridge, B. G., Bürgmann, R., Fielding, E., Hensley, S., & Schulz, W. H. (2016). Three-dimensional surface deformation derived from airborne interferometric UAVSAR: Application to the Slumgullion Landslide. *Journal of Geophysical Research: Solid Earth*, *121*, 3951–3977. https://doi.org/10.1002/2015JB012559

Dzurisin, D., Lisowski, M., & Wicks, C. W. Jr. (2017). Semipermanent GPS (SPGPS) as a volcano monitoring tool: Rationale, method, and applications. *Journal of Volcanology and Geothermal Research*, *344*, 40–51. https://doi.org/10.1016/j.jvolgeores.2017.03.007

Farinotti, D., Huss, M., Bauder, A., Funk, M., & Truffer, M. (2009). A method to estimate the ice volume and ice-thickness distribution of alpine glaciers. *Journal of Glaciology*, *55*(191), 422–430. https://doi.org/10.3189/002214309788816759

Fu, Y., Argus, D. F., & Landerer, F. W. (2015). GPS as an independent measurement to estimate terrestrial water storage variations in Washington and Oregon. *Journal of Geophysical Research: Solid Earth*, *120*, 552–566. https://doi.org/10.1002/2014JB011415

Handwerger, A. L., Roering, J. J., Schmidt, D. A., & Rempel, A. W. (2015). Kinematics of earthflows in the Northern California Coast Ranges using satellite interferometry. *Geomorphology*, *246*, 321–333. https://doi.org/10.1016/j.geomorph.2015.06.003

Hu, X., Wang, T., & Liao, M. (2014). Measuring coseismic displacements with point-like targets offset tracking. *IEEE Geoscience and Remote Sensing Letters*, *11*(1), 283–287. https://doi.org/10.1109/LGRS.%202013.2256104

Hu, X., Wang, T., Pierson, T. C., Lu, Z., Kim, J., & Cecere, T. H. (2016). Detecting seasonal landslide movement within the Cascade landslide complex (Washington) using time-series SAR imagery. *Remote Sensing of Environment*, *187*, 49–61. https://doi.org/10.1016/j.rse.2016.10.006

Huang, M.-H., Fielding, E. J., Liang, C., Milillo, P., Bekaert, D., Dreger, D., & Salzer, J. (2017). Coseismic deformation and triggered landslides of the 2016 Mw 6.2 Amatrice earthquake in Italy. *Geophysical Research Letters*, *44*, 1266–1274. https://doi.org/10.1002/2016GL071687

Iverson, R. M. (2000). Landslide triggering by rain infiltration. *Water Resources Research*, *36*(7), 1897–1910. https://doi.org/10.1029/2000WR900090

Iverson, R. M. (2005). Regulation of landslide motion by dilatancy and pore pressure feedback. *Journal of Geophysical Research*, *110*, F02015. https://doi.org/10.1029/2004JF000268

Iverson, R. M., Reid, M. E., & LaHusen, R. G. (1997). Debris-flow mobilization from landslides. *Annual Review of Earth and Planetary Sciences*, *25*(1), 85–138. https://doi.org/10.1146/annurev.earth.25.1.85

Iverson, R. M., Reid, M. E., Iverson, N. R., LaHusen, R. G., Logan, M., Mann, J. E., & Brien, D. L. (2000). Acute sensitivity of landslide rates to initial soil porosity. *Science*, *290*(5491), 513–516. https://doi.org/10.1126/science.290.5491.513

Iverson, R. M., George, D. L., Allstadt, K., Reid, M. E., Collins, B. D., Vallance, J. W., et al. (2015). Landslide mobility and hazards: Implications of the 2014 Oso disaster. *Earth and Planetary Science Letters*, *412*, 197–208. https://doi.org/10.1016/j.epsl.2014.12.020

Mackey, B. H., & Roering, J. J. (2011). Sediment yield, spatial characteristics, and the long-term evolution of active earthflows determined from airborne LiDAR and historical aerial photographs, Eel River, California. *Geological Society of America Bulletin*, *123*(7-8), 1560–1576. https://doi.org/10.1130/B30306.1

Michel, R., Avouac, J. P., & Taboury, J. (1999). Measuring ground displacements from SAR amplitude images: Application to the Landers earthquake. *Geophysical Research Letters*, *26*(7), 875–878. https://doi.org/10.1029/1999GL900138

Moore, P. L., & Iverson, N. R. (2002). Slow episodic shear of granular materials regulated by dilatant strengthening. *Geology*, *30*(9), 843–846. https://doi.org/10.1130/0091-7613(2002)030%3C0843:SESOGM%3E2.0.CO;2

Morlighem, M., Rignot, E., Seroussi, H., Larour, E., Ben Dhia, H., & Aubry, D. (2011). A mass conservation approach for mapping glacier ice thickness. *Geophysical Research Letters*, *38*, L19503. https://doi.org/10.1029/2011GL048659

Nikolaeva, E., Walter, T., Shirzaei, M., & Zschau, J. (2014). Landslide observation and volume estimation in central Georgia based on L-band InSAR. *Natural Hazards and Earth System Sciences*, *14*(3), 675–688. https://doi.org/10.5194/nhess-14-675-2014

Palmer, L. (1977). Large landslides of the Columbia River Gorge, Oregon and Washington. *Reviews in Engineering Geology*, *3*, 69–84. https://doi.org/10.1130/REG3-p69

Pierson, T. C., Evarts, R. C., & Bard, J. A. (2016). Landslides in the western Columbia Gorge, Skamania County, Washington, U.S. Geological Survey Scientific Investigations Map 3358.

Priest, G. R., Schulz, W. H., Ellis, W. L., Allan, J. A., Niem, A. R., & Niem, W. A. (2011). Landslide stability: Role of rainfall-induced, laterally propagating, pore-pressure waves. *Environmental & Engineering Geoscience*, *17*(4), 315–335. https://doi.org/10.2113/gseegeosci.17.4.315

Randall, J. R. (2012). *Characterization of the Red Bluff Landslide, Greater Cascade Landslide Complex, Columbia River Gorge, Washington*, (Master's thesis). Portland State University.

Rogers, J. D., & Chung, J. (2016). Applying Terzaghi's method of slope characterization to the recognition of Holocene land slippage. *Geomorphology*, *265*, 24–44. https://doi.org/10.1016/j.geomorph.2016.04.020

Scambos, T. A., Dutkiewicz, M. J., Wilson, J. C., & Bindschadler, R. A. (1992). Application of image cross-correlation to the measurement of glacier velocity using satellite image data. *Remote Sensing of Environment*, *42*(3), 177–186. https://doi.org/10.1016/0034-4257(92)90101-O

Tong, X., & Schmidt, D. A. (2016). Active movement of the Cascade landslide complex in Washington from a coherence-based InSAR time series method. *Remote Sensing of Environment*, *186*, 405–415. https://doi.org/10.1016/j.rse.2016.09.008

Wang, T., & Jónsson, S. (2015). Improved SAR amplitude image offset measurements for deriving three-dimensional Coseismic displacements. *IEEE Journal of Selected Topics Journal of Applied Earth Observation Remote Sensing*, *8*(7), 3271–3278. https://doi.org/10.1109/JSTARS.2014.2387865

Waters, A. C. (1973). The Columbia River Gorge—Basalt stratigraphy, ancient lava dams, and landslide dams. In J. D. Beaulieu (Ed.), *Geologic Field Trips in Northern Oregon and Southern Washington* (Vol. 77, pp. 133–162). Portland, OR: Oregon Department of Geology and Mineral Industries Bulletin.

Wise, W. S. (1961). *The geology of the wind river area, Washington, and the stability relations of celadonite*, (PhD dissertation, pp. 191–195). John Hopkins University.

Zhao, C., Lu, Z., Zhang, Q., & Fuente, J. (2012). Large-area landslide detection and monitoring with ALOS/PALSAR imagery data over Northern California and Southern Oregon, USA. *Remote Sensing of Environment*, *124*, 348–359. https://doi.org/10.1016/j.rse.2012.05.025